Surface and Electrochemical Characterization of IrTi-Oxide Coatings: Towards the Improvement of Radiopacity for Coronary Stent Applications

Sajjad Habibzadeh[1], Dominique Shum-Tim[2] and Sasha Omanovic[1,*]

[1] Department of Chemical Engineering
[2] Divisions of Cardiac Surgery and Surgical Research, Department of Surgery, McGill University, Montreal, QC, Canada
[*]E-mail: sasha.omanovic@mcgill.ca

Thin Ir_xTi_{1-x}-oxide coatings ($x = 0$, 0.2, 0.4, 0.6, 0.8 and 1) were formed on Ti substrates and commercial 316L stainless steel (SS) coronary stents employing a simple thermal deposition method. Electrochemical and surface-characterization techniques were used to investigate the surface topography/morphology and chemical composition of the coatings, their electrochemical properties, and radiopacity. These properties were found to highly depend on the coating composition; however, no particular composition-dependent trend was observed. All the coatings were found to be stable under the experimental conditions employed in the research. The electrochemical behaviour of the Ir-containing coatings was governed mostly by the pseudo-capacitive response of the coating and the coating/electrolyte interface. The absence of the low-frequency resistive component of the impedance response indicated a very high corrosion resistance of the coatings. SS coronary stents modified by Ir_xTi_{1-x}-oxide coatings were found to be more radiopaque than the bare (naked) SS stent. The $Ir_{0.4}Ti_{0.6}$-oxide coating showed to be the most uniform, the most corrosion resistant and the most radiopaque coating.

1. INTRODUCTION

Surface characteristics of a biomedical implant, such as the surface energy, texture, potential and stability, significantly influence the interaction of the implant with the surrounding biological / biochemical environment. These characteristics, and thus the implant/surrounding interactions, could be tuned by applying various surface treatment methods. Formation of coatings/films on the implant

surface has been one of the promising surface treatment methods used to alter the implant surface characteristics without interfering with the bulk properties of the implant. This approach in surface treatment is of great interest in the area of development of coronary stents [1-4]. Coronary stents are small mesh-like cylindrical 'tubes' inserted into a coronary artery at the site of the artery blockage in order to re-open the blocked site and allow blood to circulate normally [5-8]. The majority of currently used coronary stents are made of 316L stainless steel (SS). Unfortunately, although these stents offer good mechanical properties, their biocompatibility is rather poor [1, 2, 9, 10] . In addition, the radiopacity of SS stents is low, i.e. they are quite difficult to visualize under X-ray fluoroscopy while being implanted, and also post-implantation [11]. Drug-eluting stents (DESs) have been developed with the aim to increase the stent's biocompabitility. However, recent studies have shown that DES neither offer long-term benefits in comparison to bare-metal stents (BMS), nor better radiopacity [12-16].

This work aims at addressing the issue of stent's radiopacity. The radiopacity of a stent depends on the single through-wall (strut) thickness, and mass X-ray absorption coefficient of elements comprising the stent material, in this case 316L SS [3, 17]. Unfortunately, neither of the two can be changed without compromising mechanical properties of the stent. However, a convenient approach in increasing the stent's radiopacity could be to coat the entire stent surface with a very thin film of a highly radiopaque material. The other requirements that need to be met by doing this are that, the film material be of equal or better biocompatibility than the BMS surface, be corrosion resistant, and it should adhere well to the BMS surface.

In the present investigation, coatings made of Ir/Ti-oxides were used for the above purpose. Iridium oxide was chosen as the primary coating material due to its high X-ray attenuation coefficient [17], and its high inertness [8, 18] and electrochemical (corrosion) stability [19-22]. Titanium oxide was chosen as a secondary coating material due to its high electrochemical (corrosion) stability and high biocompatibility. In addition, an assumption was that by incorporating titanium oxide into the Ir-oxide based coating, the corrosion stability of the coating would increase [23, 24]. Besides a comprehensive characterization of the Ir/Ti-oxide coatings employing a range of surface characterization techniques, a quantitative analysis of the radiopacity of Ir/Ti-oxide coatings formed on commercial 316L stainless steel stents has been performed.

2. EXPERIMENTAL DETAILS

2.1. Preparation of samples

Ir_xTi_{1-x}-oxide coatings (x = 0, 0.2, 0.4, 0.6, 0.8 and 1) were formed on a flat titanium substrate or on a commercial 316L stainless steel stent surface employing a thermal method. First, a coating precursor solution was prepared by dissolution of a proper amount of $IrCl_3 \times 3H_2O$ and/or $Ti_4(OCH_3)_{16}$ in 37% HCl and isopropanol at a total metal-content concentration of 0.5 mol dm^{-3}. Depending on the desired compositions of iridium and titanium in the coating material, the appropriate amount of iridium chloride and titanium isopropoxide were dissolved in 37% HCl to yield half of the final volume of the

coating precursor solution. Then, water was added to restore the final volume. Next, the solution was heated to evaporate one-fourth of its volume, and isopropanol was added to re-establish the final solution volume.

Titanium substrates, which were used as a support for oxide films, were 12.7 mm-diameter discs machined to a thickness of 2 mm. Before the oxide film deposition, the substrates were first polished using 600-grit SiC sandpaper, and then etched in 37% HCl (1:1, v:v) at the boiling temperature for 30 min. Next, the substrates were rinsed with acetone, isopropanol and water. Metal-oxide coatings were formed on such pre-treated Ti substrates in the following way. First, a thin layer of the metal precursor solution was brushed on one side of the substrate. The substrate was then heated in an air furnace at atmospheric pressure and $500^{o}C$ for 15 min. This procedure was repeated for ten times. Finally, the sample was annealed at the same temperature for 1 hr, to convert the surface coating into a metal oxide coating. A similar procedure was used to coat a 316L stainless steel stent surface (Boston Sci., 20 mm Liberte WH) with a metal-oxide coating. However, the etching step was skipped in order to avoid thinning of the already thin stent strut wall. In addition, the precursor solution was not brushed on the stent surface, but a dip-coating method was employed using a dip coater (MTI, TL0-01 Desktop Dip Coater). A withdraw speed and immersion time of $60\,mm\,min^{-1}$ and 1 min were applied, respectively.

2.2. Surface characterization

Electron micrographs of the sample surfaces were produced using a Philips XL-30 field emission scanning electron microscope (FE-SEM). The crystallographic structure of oxide coatings was investigated by X-ray diffraction analysis (XRD) employing a Bruker D8 Discovery X-Ray diffractometer using CuKα radiation. X-ray photoelectron spectroscopy (XPS) measurements were made using a ThermoFisher Scientific K-Alpha Spectrometer equipped with an argon ion gun. The X-ray polychromatic source was AlKα (1486.6 eV). The analyzer was fixed at normal position (90°) to the surface. A survey spectrum was first recorded to identify all elements present on the sample surface, followed by recording high resolution spectra. The spectra were fitted using the CasaXPS software package (version 2.13.16) employing Shirley background subtraction and a combination of Gaussian and Lorentzian (70:30 ratio) line shapes.

2.3. Electrochemical measurement

Electrochemical measurements were carried out using an Ecochemie Autolab PGSTAT30 Potentiostat/Galvanostat, combined with the FRA2 electrochemical impedance spectroscopy (EIS) module. The GPES/FRA v.4.9.7 software was employed to control the instrument, as well as for data collection and treatment. A three-electrode electrochemical cell was used in all electrochemical measurements. A graphite rod was used as the counter electrode (CE) and the reference electrode (RE) was a saturated calomel electrode [10]. Metal-oxide coated samples of various compositions (Ir_xTi_{1-x}-oxides, $x = 0$, 0.2, 0.4, 0.6, 0.8 and 1) were used as the working electrodes (WE). In order to expose

only the coated side of the samples to the electrolyte, the WE was placed in a specially constructed electrochemical cell, exposing 0.5 cm^2 of the treated side of the WE to the electrolyte. All the electrochemical experiments were performed in an oxygen-free electrolyte, which was achieved by continuously purging the electrolyte with argon, starting 30 min prior to the measurement and continuing during the measurement. De-ionized (DI) water of resistivity of 18.2 MΩ cm was used in all experiments.

Electrochemical measurements were conducted in the following order. Frist, cyclic voltammetry (CV) experiments were performed in 0.5 M H_2SO_4 to determine a true electrochemically-active surface (TEAS) area of a sample. Then, the sample was kept at open circuit potential (OCP) in 0.16 M NaCl, which is the chloride concentration equivalent to that in human body fluids, for either a period of 1 h or until a potential was stabilized to less than a 2 mV min^{-1} change. This step was followed by electrochemical impedance spectroscopy (EIS) measurements at OCP over a frequency range of 10 mHz to 50 kHz. The AC voltage amplitude was set to 10 mV. Next, the samples were polarized by CV in 0.16 M NaCl between the H_2 and O_2 evolution region (-0.3 to 1.3 V) for 100 sweeps (ca. 17 hr of continuous potentiodynamic cycling, named here as 'torturing'), to evaluate the stability of the coating. EIS measurement was then performed at OCP to analyze the coating condition after being tortured.

2.4. Radiopacity analysis

To evaluate the radiopacity of the coated 316L stainless steel stents, X-ray images were obtained using an X-ray unit in which the focus was positioned perpendicular to the samples. The X-ray machine was set to operate at 80 kV and 3.19 mA s, and at a focus-sample distance of 100 cm, in accordance with the ASTM-F 640 (Standard Test Methods for Determining Radiopacity for Medical Use) [25]. As a reference, an aluminum step-wedge (98% purity) with a thickness range from 1 to 9 mm (with 1 mm increments) was first imaged. Then, a transmission densitometer was used to measure the corresponding optical density value. The resultant optical density values were further calibrated with gray scale values which were accurately calculated by image processor software (Image J). It should be mentioned that the number of gray shades in the digital image is determined by the number of binary digits (bits) used to define a pixel. Depending on the system, the gray values could be from 8- to16-bit. The darkest gray shade ('black') is usually defined by the zero value, while the brightest ('white') has, for an 8-bit system for example, a value of 255. Gray scale values of digital X-ray images taken at different locations of the stent were calculated by the software program. Subsequently, the optical density values of each specimen were calculated using the provided calibration curve.

3. RESULTS AND DISCUSSIONS

3.1. Surface Topography

Fig. 1 shows the representative SEM images displaying the microstructure of iridium/titanium oxide coatings of different compositions. The images evidence the presence of small crystallites

separated by micro-cracks, rendering the surface relatively rough. The sample coated by pure titanium oxide (Fig. 1a) displays the "cracked-mud" morphology [16,18], characterized by the existence of larger micro-cracks.
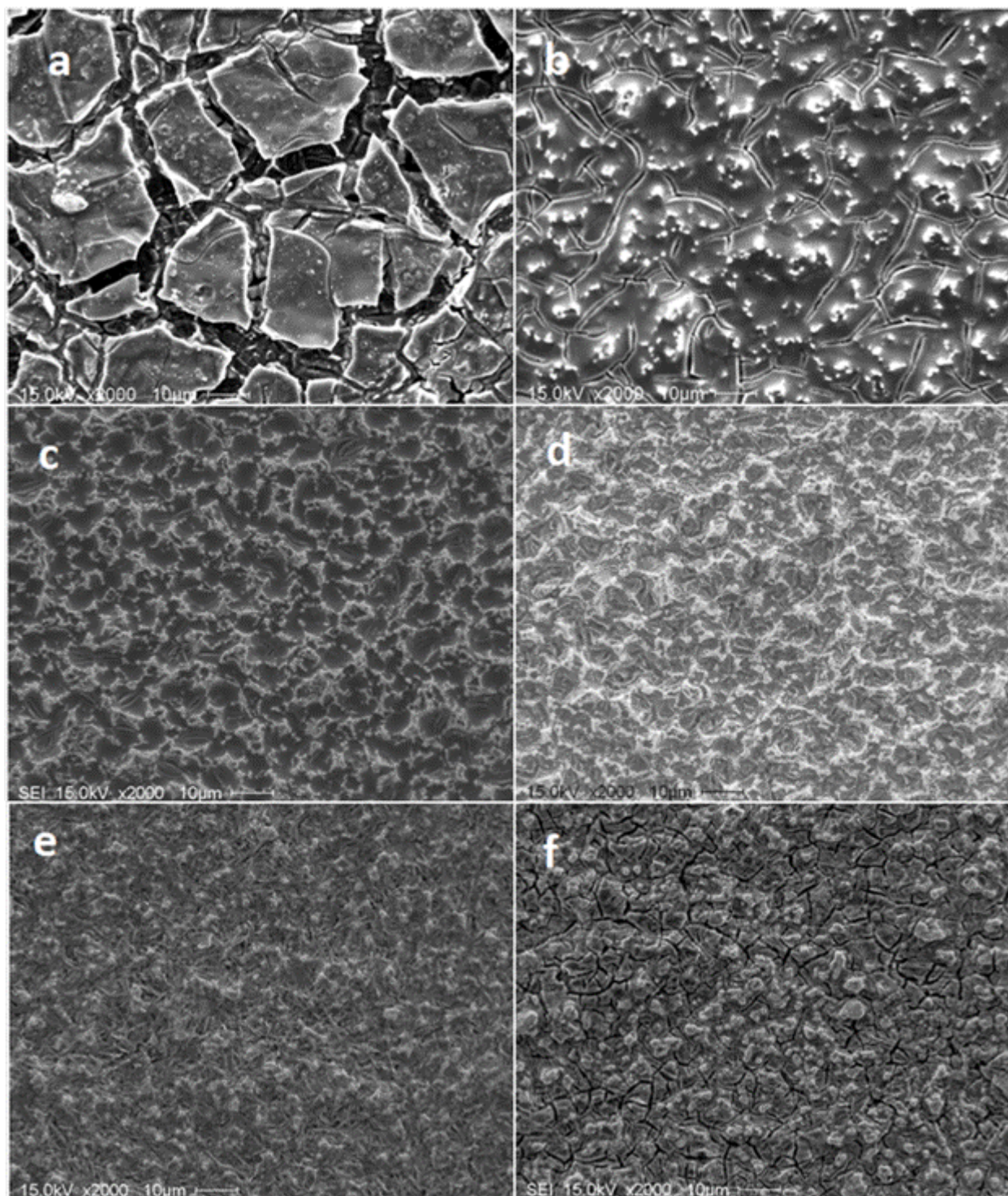
Figure 1. SEM micrographs of Ir_xTi_{1-x} oxide coatings formed on a Ti substrate. (a) x=0, (b) x=0.2, (c) x=0.4, (d) 0.6, (e) x=0.8, and (f) x=1.

However, with an increase in Ir content in the coating, the morphology of the surface changes; the size of the cracks diminishes up to the Ir content of 40% (Fig. 1c), and then slightly increases yielding again a "cracked-mud" morphology for the pure Ir-oxide coating (Fig. 1f). The analysis of cross-section images of the coatings has revealed that all the coatings are of a very similar thickness, 1.8 ±0.4 μm.

Dark area:
Ir: 34.5%
Ti: 65.5%

Bright area:
Ir: 60.3%
Ti: 39.7%

15.0kV x50000 0.5μm
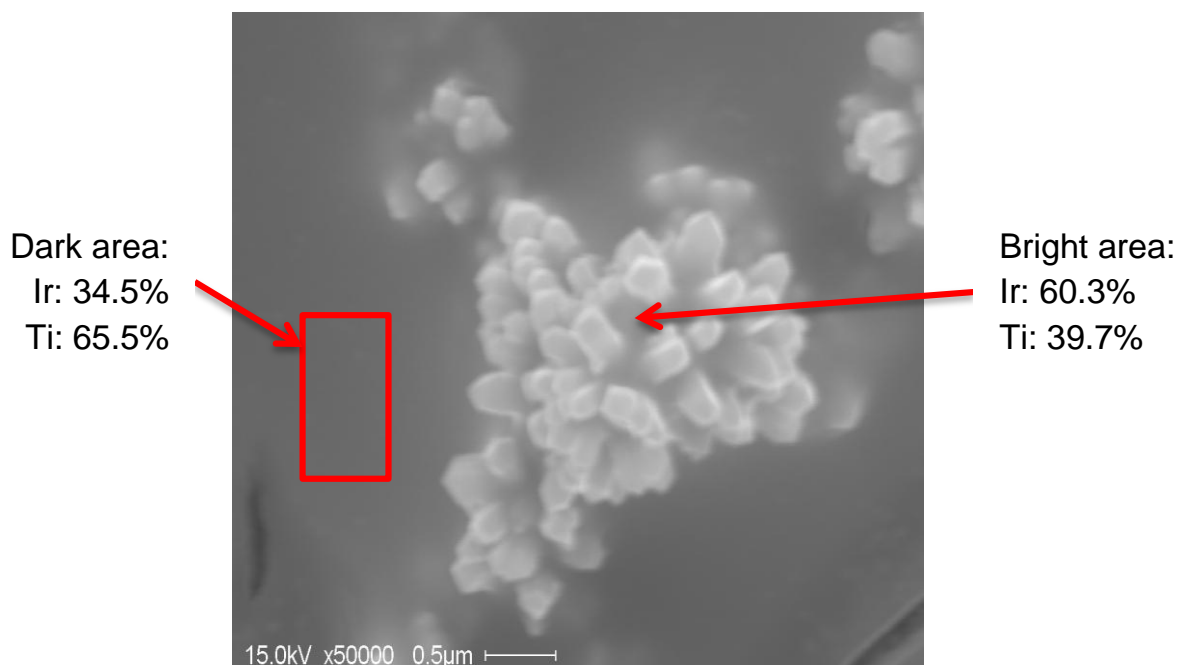
Figure 2. SEM image of the $Ir_{0.4}Ti_{0.6}$-oxide coating depicting an isolated crystallite structure. These structures are uniformly spread across the entire coating surface, as seen in Fig. 1c. The corresponding Ir and Ti content obtained by EDX is also shown. The values represent mean values obtained by analysis of many similar features on the surface (bright and dark areas).

EDX analysis of the coatings was performed at various locations on the surface. The results indicated that the actual average metal composition of the coatings was in good agreement with the nominal values. However, variations in the local composition of the coatings were noted. For example, the SEM image in Fig. 2 shows a selected surface crystallite feature on the $Ir_{0.4}Ti_{0.6}$-oxide coating surface. Such features are uniformly distributed across the surface (Fig. 1c). The EDX analysis revealed that the bright areas (crystallite features) are enriched with Ir (60.3 ±2.1%), in comparison to both the nominal content (40%) and dark areas (34.5±1.4%).

3.2. Crystalline Structure

The structural identification and changes in crystallinity of the metal-oxide coatings as a function of composition were investigated by XRD, Fig. 3. The results show that the crystalline planes of tetragonal iridium oxide become more intense with an increase in iridium content in the coating. In

addition, the peaks corresponding to the anatase phase of titanium oxide only exist for the pure titanium oxide coating, while by adding iridium into the coating, the anatase phase changes to the rutile one. The Scherrer formula [26-28] was applied on the (1 1 0) diffraction peak to calculate the corresponding crystallite size, and they ranged from 8.1 nm to 10.2 nm for the Ir_xTi_{1-x}-oxide compositions ranging from x = 0.2 to x = 1.
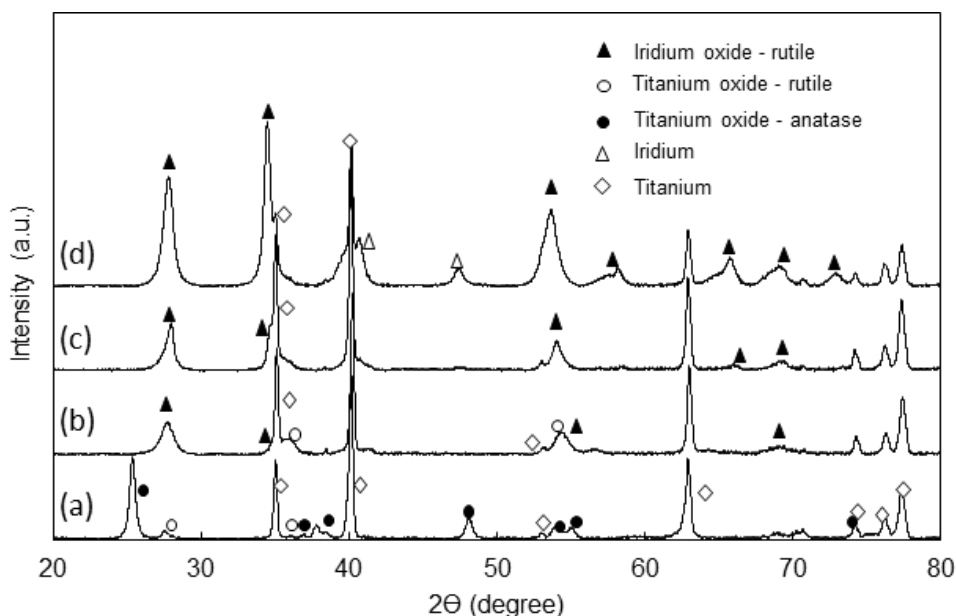
Figure 3. X-ray diffraction pattern of Ir_xTi_{1-x}-oxides coatings: (a) x=0, (b) x=0.2, (c) x=0.4, and (d) x=1.

In addition, the shift of the diffraction peaks of the Ir-oxide rutile-type phase with the change in the composition of iridium/titanium oxides reveals that the corresponding lattice constants vary with an increase in iridium content, indicating the solid solution of the Ir_xTi_{1-x}-oxides.

3.3. Surface Chemical Composition

The XPS analysis of Ir_xTi_{1-x}-oxide coatings was performed in order to investigate their surface chemical composition. To identify all elements in the coating material, general survey spectra were first recorded. Fig. 4a shows a representative XPS survey spectrum of the $Ir_{0.4}Ti_{0.6}$-oxide coating surface. Traces of carbon can be observed as the only contamination present on the coating surface. The other elements are Ir, Ti and O.

The corresponding resolved (deconvoluted) Ir 4f core level photoemission spectrum is presented in Fig. 4b. To analyze the Ir 4f core level by curve fitting, the values of the full-width-at-half-maximum (FWHM) of the spin-orbit doublet were equalized, which consequently resulted in the ratio of component intensities of $Ir4f_{7/2}$ to $Ir4f_{5/2}$ approaching ca. 4:3. A very good agreement between the modeled (solid line) and experimental spectrum (dotted line) was obtained. The binding energy

(B_E) of major and minor Ir $4f_{7/2}$ photoelectron lines are located at 61.9±0.1 eV and 63.3±0.1 eV, respectively. The Ir $4f_{5/2}$ peak appears at 64.9±0.1 eV. The B_E values of the Ir 4f doublet, 61.9±0.1 and 64.9±0.1 eV, correspond to the binding energies characteristic of anhydrous oxide, IrO_2 [29-33]. In addition, the binding energy shift of the minor Ir $4f_{7/2}$ photoemission by 1.4 eV seems to be close to the literature-reported value of 1.2 eV, for iridium oxide [34].
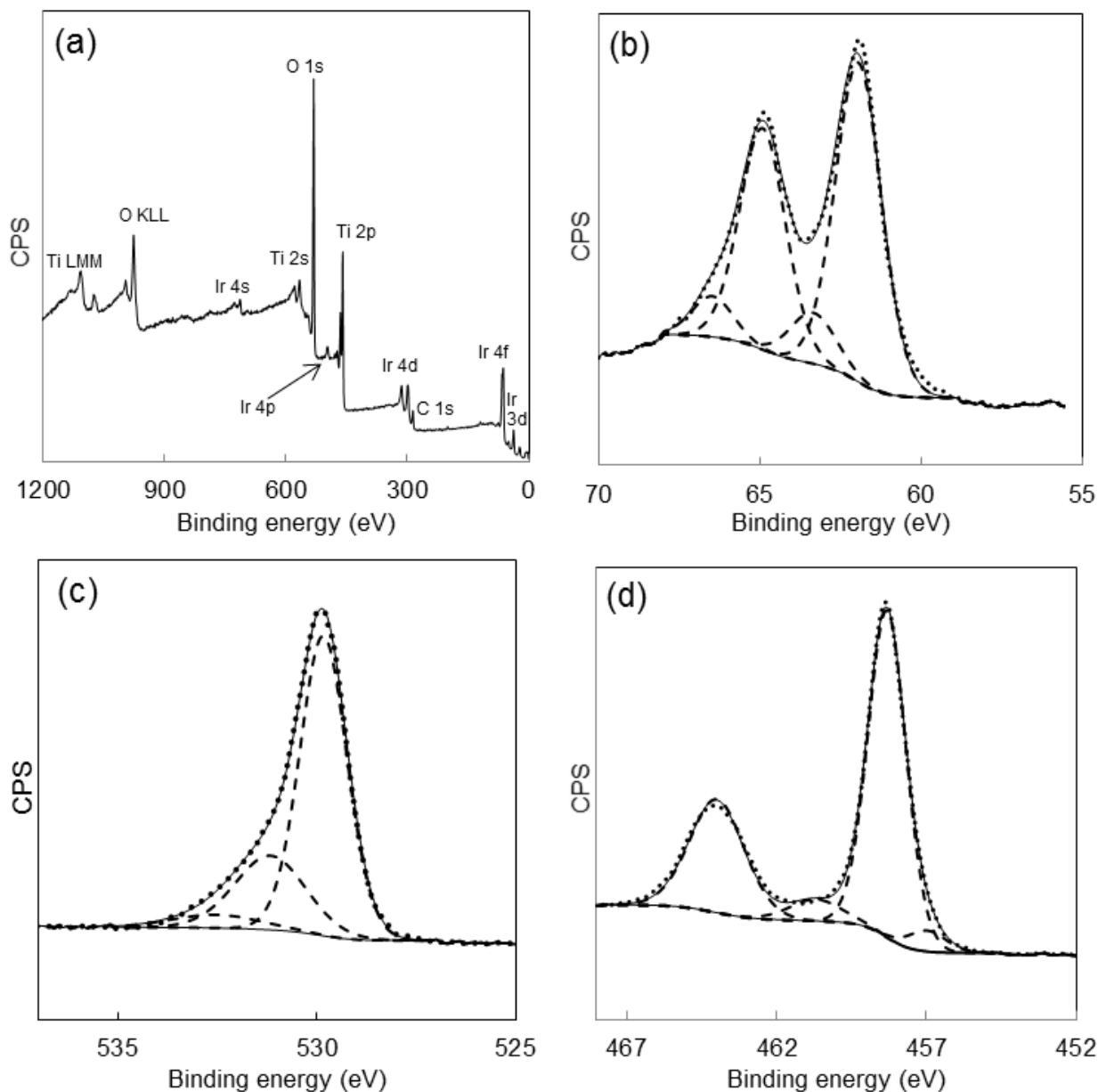
Figure 4. XPS spectra of a $Ir_{0.4}Ti_{0.6}$-oxide coating surface: (a) general survey spectrum, and deconvoluted spectra of (b) iridium, (c) oxygen, and (d) titanium. Dots represent the experimental spectrum and the solid line represents the corresponding simulated spectrum. The denconvoluted contributions are presented by dashed lines.

It should be mentioned that there are controversies related to the nature of the extra Ir 4f doublet and the satellite peak at 66.4±0.2 eV [32, 33, 35]; nonetheless, it is attributed to the final state screening response with no chemical back up [22, 29, 31, 36, 37].

Fig. 4c exhibits an O1s photoelectron response fitted to three different oxygen species. The first resolved peak at 529.8±0.2 eV is assigned to the metal oxide, whereas the peak at 531.1±0.2 eV corresponds to the overlapped contribution of metal hydroxide and carbonyl oxygen [31, 38]. The third response at 532.5±0.3 might be attributed to the oxygen atom of water [38, 39].

A high resolution spectrum of the Ti 2p region of the $Ir_{0.4}Ti_{0.6}$-oxide coating surface is shown in Fig. 4d. Considering the different oxidation states of titanium, the Ti 2p region can be fitted to several contributions, each encompassing a doublet of $2p_{3/2}$ and $2p_{1/2}$ peaks. The main doublet composed of two symmetric peaks appears at 458.3±0.2 eV and 464±0.1 eV, corresponding to the Ti^{4+} oxidation state in TiO_2 [40, 41]. Apart from the Ti^{4+} doublet, as the major feature of titanium spectrum, one can find a minor contribution of Ti^{2+} from TiO at 456.5±0.3 eV and 461.1±0.4 eV [42].

Table 1. Molar percentage of Ir in Ir_xTi_{1-x}-oxide coatings. Nominal values refer to the desired Ir content in the metal precursor salt. ICP values refer to the actual measured concentration of Ir in the coating precursor solution. XPS values refer to the Ir content on the surface of the coating. Uncertainty values: (a) ±0.1, (b) ±0.3.

Iridium content, mol %		
Nominal	ICP[a]	XPS[b]
0	-	-
20	17	15
40	35	21
60	54	37
80	76	65
100	92	81

The same analysis was performed for all Ir_xTi_{1-x}-oxide coatings (results not shown). Then, the surface content of iridium was calculated from XPS measurements and compared to the concentration of iridium in the coating precursor solution; the latter obtained by inductively coupled plasma (ICP) analysis (Table 1). The results demonstrate that there is depletion in iridium at the coating surface. This is in line with the literature [22-24, 40], and can be related to the different reactivity of two metal precursors towards oxygen. Namely, it has been thermodynamically proven that the affinity of titanium towards oxygen is much larger (ca. 7 times) than that of iridium [43]. This is most obvious for the 100% pure Ir-oxide coating; the Ti content on the surface of this coating is not zero, as one would expect, but it is 19%. Since no titanium was present in the corresponding precursor solution, the source of the surface content of titanium is the underlying titanium substrate. Practically, during the formation of the 100% Ir-oxide coating, the surface of the titanium substrate partially corrodes (dissolves). The dissolved titanium ions diffuse towards the outer coating/air interface and react with oxygen, forming Ti-oxide.

3.4. Electrochemical characterization

Fig. 1 shows that the chemical composition of the Ir_xTi_{1-x}-oxide coatings studied determines their surface morphology. Accordingly, one could expect that their electrochemical / corrosion properties would also vary. Hence, electrochemical measurements were performed to investigate electrochemical and corrosion (stability) properties of the formed coatings.
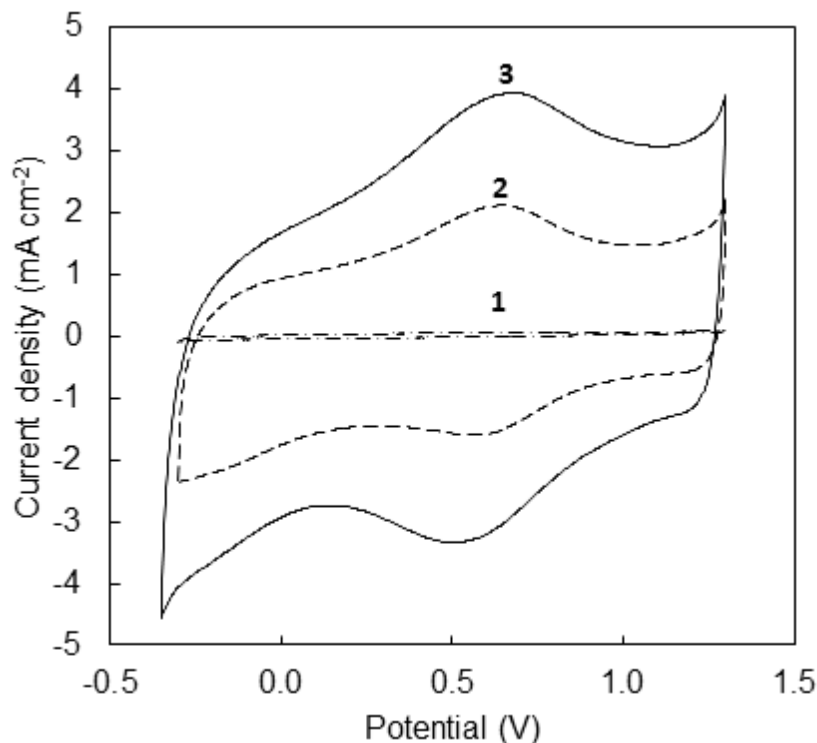
Figure 5. Cyclic voltammograms of Ir_xTi_{1-x}-oxide coatings recorded in 0.5 mol dm^{-3} H$_2$SO$_4$. Scan rate = 100 mV s^{-1}. (1) Ti-oxide, (2) $Ir_{0.2}Ti_{0.8}$-oxide, and (3) $Ir_{0.4}Ti_{0.6}$-oxide coating.

Fig. 5 displays a set of selected cyclic voltammograms (CVs) of Ir_xTi_{1-x}-oxide coatings (x = 0, 0.2 and 0.4) recorded in the potential region of water stability from -0.3 to 1.3 V in 0.5 M H$_2$SO$_4$. The wide anodic and cathodic peak centered at ca. 0.6 V and 0.55 V, respectively, can be related to the reversible Ir^{3+}/Ir^{4+} redox transition [44, 45]. This solid-state redox transition occurs with the participation of proton exchange between the oxide/OH surface groups and the solution [46, 47]:

$$M(OH)_xO_y + \delta H^+ + \delta e^- \leftrightarrow M(OH)_{x+\delta}O_{y-\delta} \tag{1}$$
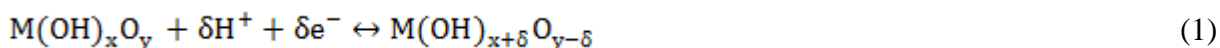
XPS results presented in Fig. 4c confirmed the presence of OH groups on the coating surface, and XPS depth-analysis results of the coating (not shown) also confirmed the presence of OH groups in the bulk of the coating. Further, Fig. 5 shows that the two Ir-containing oxide coatings show a significantly higher current response than the Ti-oxide coating. Two factors can contribute to this: The surface area effect (extrinsic effect) and the Ir^{3+}/Ir^{4+} redox transition effect (intrinsic effect). If the

latter is predominant, then the variation in the coating composition should result in the parallel variation in the current response.

To distinguish the contribution of the two effects, the true electrochemically-active surface (TEAS) area of the investigated Ir_xTi_{1-x}-oxide coatings was first determined from scan-dependent CV measurements (not shown). With an increase in the scan rate, the current response also increased. In order to determine the TEAS area of the coating, a dependence of current recorded at constant potential on the corresponding scan rate was analyzed.
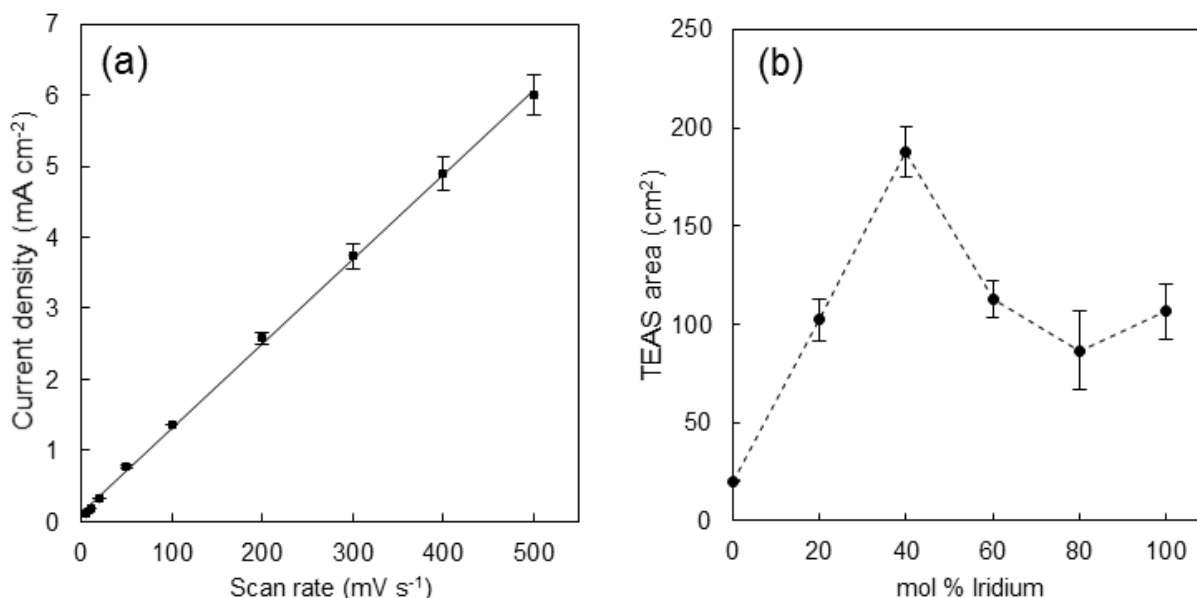

Figure 6. (a) Dependence of current at constant potential on the scan rate for the $Ir_{0.4}Ti_{0.6}$-oxide coating obtained from CV measurements performed in 0.5 M H_2SO_4. The data represent mean anodic current values recorded at three different potentials (0, 0.2 and 1 V) employing three $Ir_{0.4}Ti_{0.6}$-oxide coating samples. (b) True electrochemically-active surface (TEAS) area of Ir_xTi_{1-x}-oxide coatings ($0 \leq x \leq 1$).

Fig. 6a is an example of the behavior obtained for the $Ir_{0.4}Ti_{0.6}$-oxide coating. The slope of the line in Fig. 6a can be related to the electrochemical differential capacitance of the $Ir_{0.4}Ti_{0.6}$-oxide/solution interface. An average value of 11±0.85 mF was obtained for this specific coating composition. This value is taken to be proportional to the TEAS area of the $Ir_{0.4}Ti_{0.6}$-oxide coating. Now, comparing this value to a theoretical differential capacitance value for metal oxides, 60 $\mu F\,cm^{-2}$ [48-50], the TEAS area of the $Ir_{0.4}Ti_{0.6}$-oxide coating was calculated to be 188±13 cm^2. Fig. 6b presents the TEAS area values for all the investigated Ir_xTi_{1-x}-oxide coating compositions. No particular trend with the coating composition can be observed. However, one can notice that the largest TEAS area was obtained for the $Ir_{0.4}Ti_{0.6}$-oxide coating which is characterized by the absence of large micro-cracks (Fig. 1c).

The area under the anodic curve of the CVs in Fig. 5 represents the total anodic charge [51] delivered during the anodic sweep, and that under the cathodic CV curve represents the total cathodic charge. The anodic and cathodic charge depends on the two (extrinsic and intrinsic) effects mentioned

earlier. Fig. 7a shows the total anodic charge density (normalized with respect to the geometric area of the coating surface) as a function of the metal-oxide coating composition. It can be seen that the total charge density value reaches a maximum value for the $Ir_{0.4}Ti_{0.6}$-oxide coating. Now, when the values presented in Fig. 7a are normalized with respect to the TEAS area of the coating (Fig. 6b), a trend presented in Fig. 7b results.
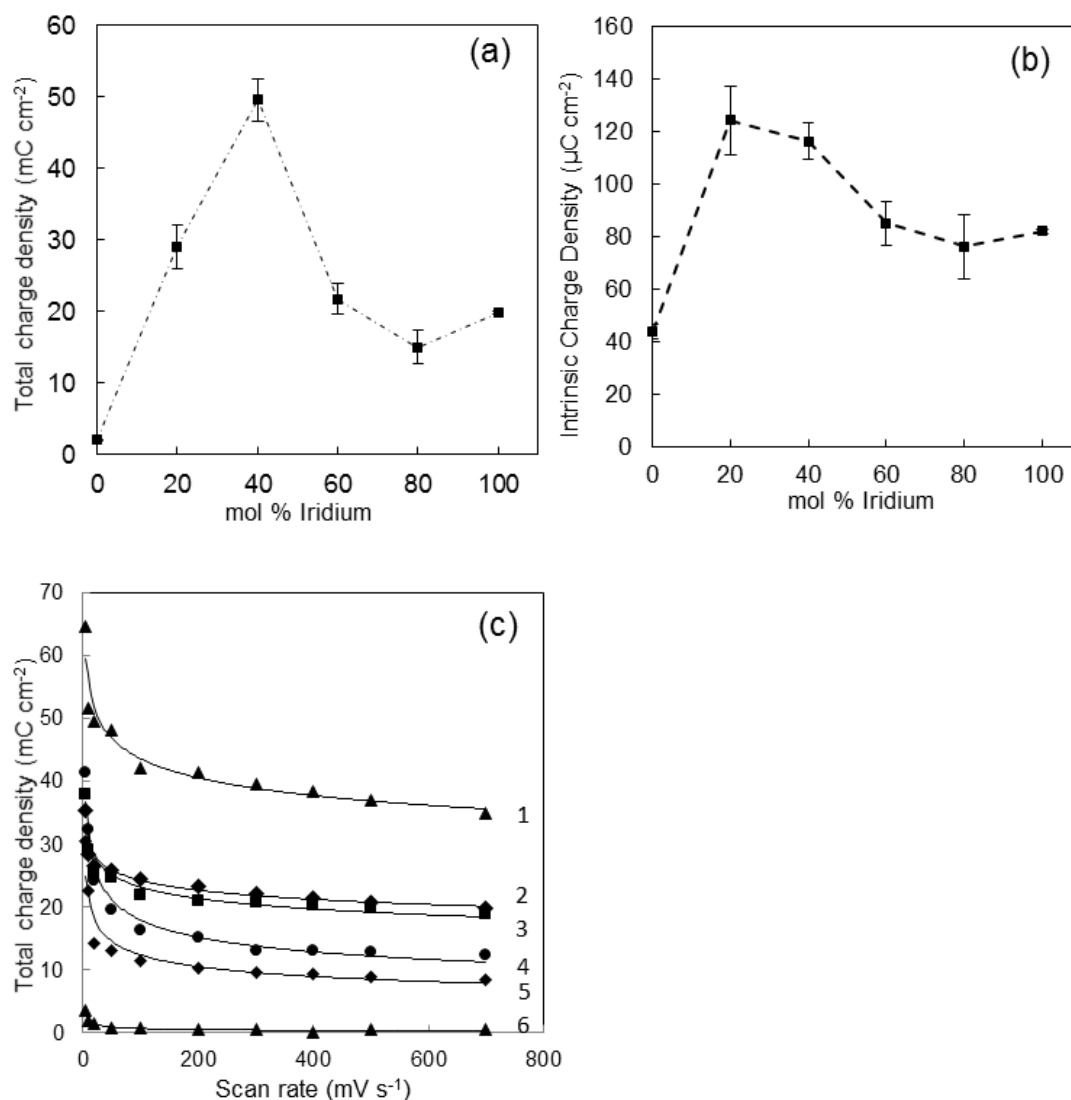
Figure 7. (a) Total anodic charge density (intrinsic + extrinsic) as a function of Ir_xTi_{1-x}-oxide coating composition obtained from CVs recorded in 0.5 M H_2SO_4 at a scan rate of 10 mV s^{-1} and in the potential region from -0.3 to 1.3 V. (b) The same as in (a), but the values are normalized with respect to the TEAS area of the coating presented in Fig. 6b, thus yielding only the intrinsic charged density. (c) Dependence of total anodic charge density on scan rate applied during the electrode cycling in 0.5 M H_2SO_4 and in the potential region from -0.3 to 1.3 V, for various compositions of Ir_xTi_{1-x}-oxides, (1) x=0.4, (2) x=0.6, (3) x=0.2, (4) x=1, (5) x=0.8, and (6) x=0.

This trend represents the dependence of the intrinsic charge density on the coating composition, and is thus related solely to the electrochemical (redox) properties of the coatings. Although the trends in Figs. 7a and 7b seem similar, a maximum in the intrinsic charge delivery is yielded by the $Ir_{0.2}Ti_{0.8}$-oxide coating, which was surprising. Namely, the assumption was that the intrinsic charge delivery for

Ir_xTi_{1-x}-oxide coatings depended mostly on the Ir^{3+}/Ir^{4+} reversible transition and that it would, therefore, increase proportionally with the increase in Ir content in the coating. The result in Fig. 7b indeed shows that when at least 20% of Ir is present in the coating, the intrinsic charge is significantly higher than that of pure titanium oxide, which demonstrates the contribution of the Ir^{3+}/Ir^{4+} redox transition. However, the overall trend in Fig. 7b does not support the role of the Ir^{3+}/Ir^{4+} reversible transition as the only factor influencing the intrinsic charge delivery, indicating that some other intrinsic effects also play a role. These effects could include changes in the electrical properties of the coatings, such as the electronic (semi)conductivity, Ti/Ir crystal-structure-dependent interactions, and surface energy and charge distribution. However, further research is needed to investigate the influence of these (and possibly some more) effects on the intrinsic charged delivery of the Ir_xTi_{1-x}-oxide coatings.

Another interesting behavior related to the total charge delivery of Ir_xTi_{1-x}-oxide coatings is presented in Fig. 7c. This plot shows the dependence of total charge density on the scan rate applied during the cyclization of the electrode. With an increase in scan rate, the total charge density decreases first rapidly, and then it gradually approached a semi-constant (plateau) value. This behavior can be related to the depth-dependent response of the coating [52, 53]. Namely, the measured charge depends on both the amount of proton exchanged between the oxide coating and the aqueous solution (Eq. (1)) and on the electrochemical double-layer charge. However, the latter is not scan rate dependent. On the other hand, due to the participation of the proton in Eq.(1), the charge associated with this reaction is dependent on the proton availability at the reaction site, the latter being dependent on the rate of proton diffusion within the oxide phase [53]. Thus, as the scan rate increases, the access of protons to regions deeper beneath the oxide surface becomes more difficult, and the charge measured represents the response of the oxide film closer to the outer film surface. Hence, at some infinitely high scan rate one would measure only the response of the outer oxide film surface. On the other hand, at infinitely small scan rates, one would measure the response of the entire oxide film.

3.5. Coating stability

The stability of produced Ir_xTi_{1-x}-oxide coatings was tested next in 0.16 M NaCl. The testing involved recording an electrochemical impedance spectroscopy (EIS) response of a freshly-prepared coating, followed by the coating "torturing", and then by the repetition of the EIS experiment to compare the response of the coating before and after torturing. The torturing step involved cyclic polarization of the coating in a corrosive solution of 0.16 M NaCl at a scan rate of 10 mV s^{-1} in a wide potential window, encompassing both the hydrogen and oxygen gas evolution regions. Fig. 8 shows CVs recorded in the first and the hundredth cycle for a selected coating ($Ir_{0.4}Ti_{0.6}$-oxide). The responses of the first and hundredth cycles are almost overlaid, indicating that no changes in the coating electrochemical properties occurred as a result of torturing. Similar behaviour was obtained with other coating compositions (not shown). This indicates that the coatings are very stable under the experimental conditions applied.
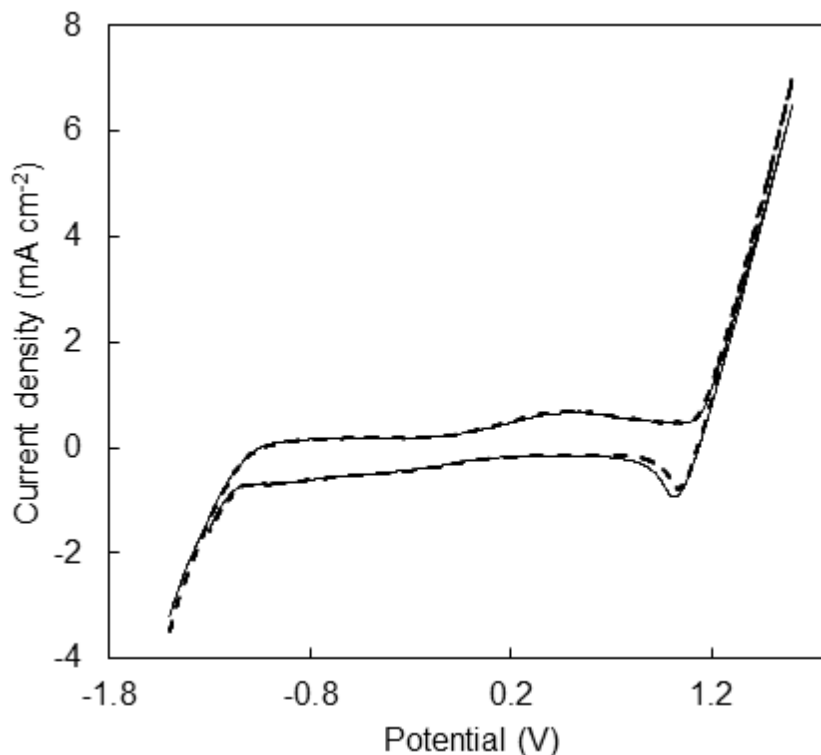
Figure 8. Cyclic voltammograms of a $Ir_{0.4}Ti_{0.6}$-oxide coating recorded in 0.16 M NaCl at a scan rate of 10 mV s^{-1}. Solid line represents the 1st sweep and the 100th sweep is presented by a dashed line. The experiment lasted ca. 17 hours, and in the text it is termed as the 'torturing' experiment.
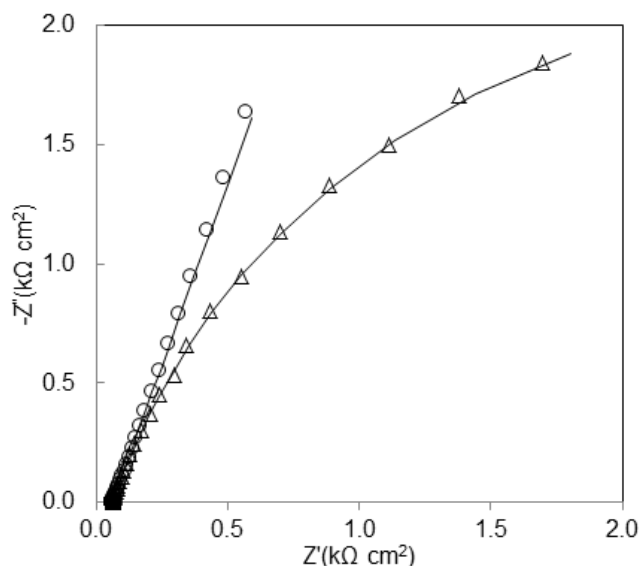
Figure 9. Nyquist plot of a (Δ) Ti-oxide, and (o) $Ir_{0.4}Ti_{0.6}$-oxide coating. The spectra were recorded in 0.16 M NaCl at OCP before the 'torturing' procedure.

To obtain quantitative values related to the coating's (general corrosion) stability, electrochemical impedance spectroscopy (EIS) measurements were made at open circuit potential (OCP) before and after torturing and the corresponding spectra were modeled using an appropriate equivalent electrical circuit (EEC) model. Fig. 9 (symbols) shows the experimental EIS spectra of Ti-

oxide (triangles) and $Ir_{0.4}Ti_{0.6}$-oxide (circles) coating samples recorded before torturing. The circular-like EIS spectrum of the Ti-oxide coating reveals the contribution of a resistive component of impedance at low frequencies, indicating a finite corrosion resistance of the sample. However, the EIS spectrum of the $Ir_{0.4}Ti_{0.6}$-oxide coating is linear (circles) and steep, indicating the absence of the low-frequency resistive behavior. This indicates the dominance of the capacitive behavior of the coating which, in turn, indicates a very high corrosion resistance of the oxide coating. A similar behavior (the absence of the low-frequency resistive contribution) was recorded on all other Ir-containing coatings.
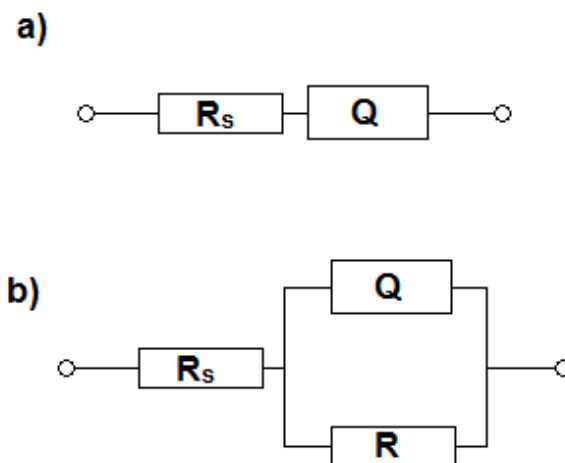
Figure 10. Equivalent electric circuits used to model the EIS data of (a) Ir_xTi_{1-x}-oxide coatings (x = 0.2, 0.4, 0.6, 0.8 and 1), and (b) a Ti-oxide coating. R_s represents the ohmic resistance of the electrolyte between the working and reference electrode; Q is the constant phase element that represents capacitance of the coating/solution interface; R is the polarization transfer resistance representing the resistance of the coating to corrosion.

In order to further verify the above observations, the experimental EIS data in Fig. 9 were modeled using non-linear least square fit analysis software and the appropriate EECs is presented in Fig. 10. The EEC in Fig. 10a was used to model the EIS response of Ir-containing coatings, while the EEC in Fig. 10b was used to model the response of the Ti-oxide coating. The meaning of the EEC elements is outlined in the figure caption. However, it should be noted that instead of pure capacitance, a constant phase element [51] was used. This is due to the distribution of the relaxation times as a result of heterogeneities present at the micro level, such as surface roughness (Fig. 1)[54]. The average value of the exponent of constant phase element [51] was 0.80±0.02, which justifies the use of Q as a capacitor.

Fig. 9 shows that a good agreement between the experimental (symbols) and simulated data (lines) is obtained when the EECs in Fig. 10 were used in the modeling procedure. This validates the above observations and demonstrates the applicability of the two EEC models in describing the EIS response of the two samples. The analysis of the values of obtained EEC parameters would not provide useful information regarding the corrosion resistance of the coatings due to the absence of the low-frequency resistive contribution, and is, therefore, omitted here.
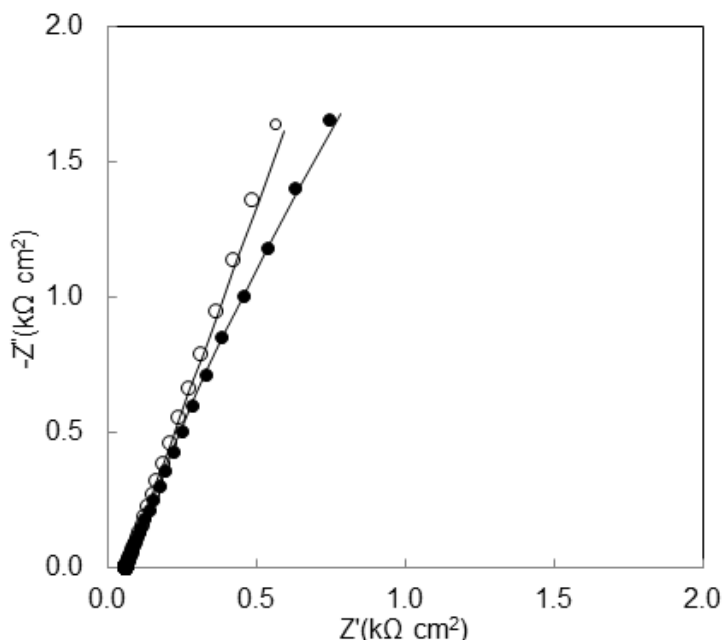
Figure 11. Nyquist plot of $Ir_{0.4}Ti_{0.6}$-oxide coating (○) before and (●) after cyclic polarization (torturing) at 10 mV s^{-1} for 17 hr in 0.16 M NaCl.

Figure 11 presents the Nyquist plot recorded on the $Ir_{0.4}Ti_{0.6}$-oxide coating before and after cyclic voltammetry (torturing). One can observe that there is not much difference in the EIS behavior of the oxide coating before and after torturing, which is in agreement with the stability results obtained by cyclic voltammetry (Fig. 8). Similar behavior was obtained with other Ir-containing coatings studied in this work. In conclusion, the previous section demonstrates that the produced Ir_xTi_{1-x}-oxide coatings are quite stable on the substrate.

3.6. Radiopacity

Given that 316L stainless steel stents have rather low radiopacity, it is thus difficult to visualize them with X-ray fluoroscopy during implantation, and also post-implantation. However, Ir-oxides offer high radiopacity. Hence, we hypothesized that by coating 316L stainless steel stents with Ir_xTi_{1-x}-oxide coatings, it would be possible to increase the stent's radiopacity, i.e. visibility under X-ray fluoroscopy. In order to test the hypothesis, commercial 316L stainless steel coronary stents were coated with the Ir_xTi_{1-x}-oxide coatings investigated here, and their resulting radiopacity was determined. The experimental procedure used is detailed in the experimental section of the paper.

First, a calibration curve was made using an aluminum step-wedge standard (inset to Fig. 12a) and a densitometer. The corresponding results are presented in Fig. 12a (main plot), which relate the optical density to the gray scale value (pixel value).
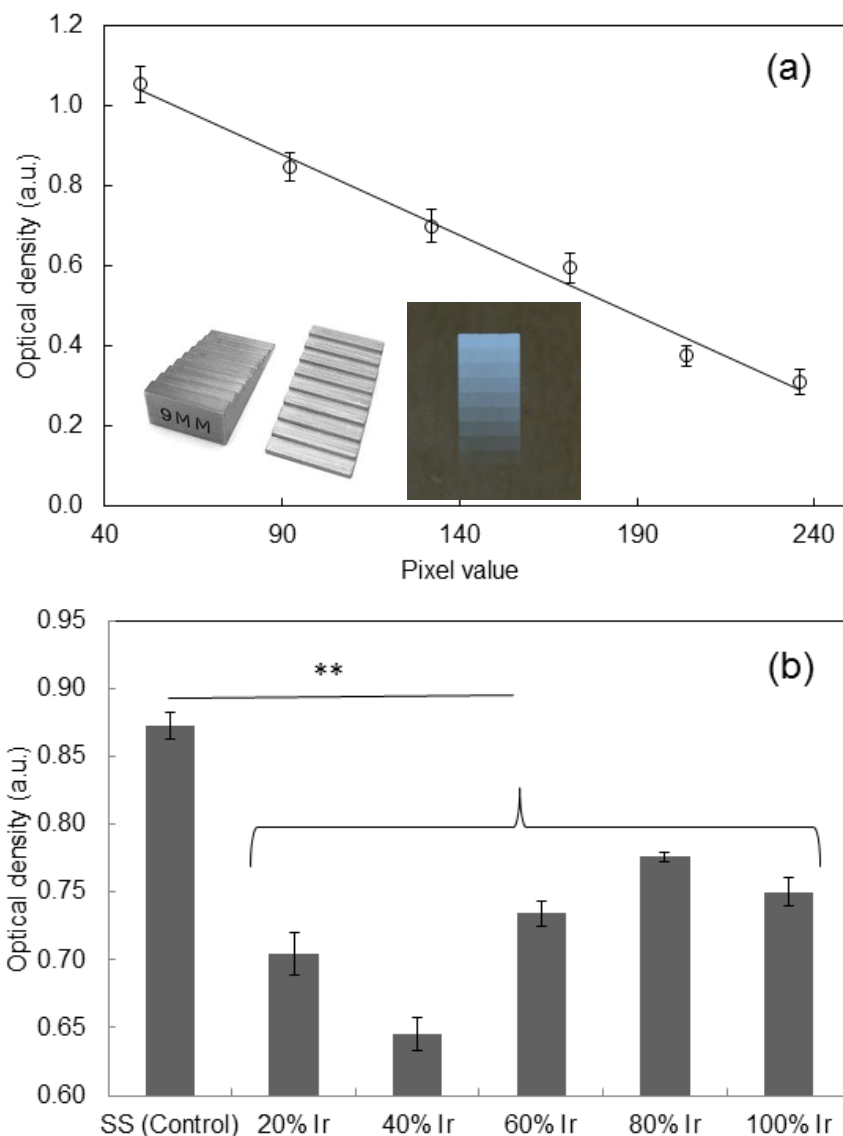
Figure 12. (a) Optical density calibration curve. The density values of the aluminum step-wedge calibration standard (inset to the figure) were measured by a densitometer and the corresponding gray scale values (pixel values) were obtained by image analysis. (b) Optical density values of Ir_xTi_{1-x}-oxide coated stents (a lower value corresponds to higher visibility under X-ray fluoroscopy, i.e. to higher radiopacity).

It should be noted that the higher the optical density value, the lower the visibility under X-ray fluoroscopy (i.e. the lower the radiopacity). It should also be mentioned that the last three thick steps on the step-wedge gave pixel values out of the range (max. 255), and are thus excluded from the calibration plot.

Using the calibration plot in Fig. 12a, the optical density of the Ir_xTi_{1-x}-oxide coated stents was measured, and presented in Fig. 12b. The result demonstrate that all the Ir_xTi_{1-x}-oxide coated stents offer statistically ($p < 0.01$) better radiopacity than the control sample (bare metal stent). A stent coated with the $Ir_{0.4}Ti_{0.6}$-oxide coating is the most radiopaque, and thus the most visible under X-ray

fluoroscopy. Knowing that titanium offers very low radiopacity, this was a surprising result since it was expected that the 100% pure Ir-oxide coating would be most radiopaque. However, it appears that the optical density of the coatings, and thus their radiopacity, does not depend only on the content of Ir in the coating, but also on the microstructure and morphology of coating arising from interaction of iridium and titanium oxides in the coating material. It would be interesting to mention that our *in-vitro* and *in-vivo* experiments with endothelial- and smooth-muscle cells, platelets, and animal models (to be presented in a separate publication) have also demonstrated that the $Ir_{0.4}Ti_{0.6}$-oxide coating is the most biocompatible coating, and thus the best candidate, among the investigated coatings, for the modification of coronary stent surfaces.

4. CONCLUSIONS

Thin Ir_xTi_{1-x}-oxide coatings were formed on flat Ti substrates and commercial 316L stainless steel coronary stents employing a simple thermal deposition method. The surface topography/morphology of the coatings was found to highly depend on the coating composition. Consequently, the total electrochemically-active surface (TEAS) area of the coatings was found to be composition dependent. The coatings were found to be of a crystalline structure. A relative surface enrichment with titanium was detected by XPS analysis. The electrochemical behaviour (charge delivery) of the coatings was dependant on both the TEAS area (extrinsic effect) and the Ir^{3+}/Ir^{4+} redox transitions (intrinsic effect). However, no particular composition-dependant trend was observed. The total (intrinsic + extrinsic) charge delivered by the coatings was found to be scan-rate dependant, indicating that the intrinsic contribution to the total charge is dependant on the rate of ion transport (within the coating). The coatings were proved to be stable, and withstood a 17-hour electrochemical 'torturing'. Finally, it was shown that commercial 316L stainles steel coronary stents modified by Ir_xTi_{1-x}-oxide coatings were more radiopaque than the bare (naked) stent. Specefically, $Ir_{0.4}Ti_{0.6}$-oxide coating was found to be the most uniform, the most corrosion resistant and the most radiopaque coating, also offering the largest TEAS area and total charge delivery.

References

1. M.N. Babapulle and M.J. Eisenberg. *Circulation.* 106 (2002) 2734.
2. M.N. Babapulle and M.J. Eisenberg. *Circulation.* 106 (2002) 2859.
3. C. Di Mario, E. Grube, Y. Nisanci, N. Reifart, A. Colombo, J. Rodermann, R. Muller, S. Umman, F. Liistro, M. Montorfano, and E. Alt. *Int. J. Cardiol.* 95 (2004) 329.
4. J. Al Suwaidi, P.B. Berger and D.R. Holmes, *Jr. J. Am. Med. Assoc.* 284 (2000) 1828.
5. C.T. Dotter. *Invest. Radiol.* 4 (1969) 329.
6. J. Palmaz. Cardiovasc. *Intervent. Radiol.* 15 (1992) 279.

7.   G. Mani, M.D. Feldman, D. Patel and C.M. Agrawal. *Biomaterials*. 28 (2007) 1689.
8.   F.A. Sgura, C. Di Mario, F. Liistro, M. Montorfano, A. Colombo and E. Grube. *Herz*. 27 (2002) 514.
9.   C. Rogers and E.R. Edelman. *Circulation*. 91 (1995) 2995.
10. D.E. W Casscells, and J T Willerson. *Texas Heart Inst J*. 21 (1994) 68.
11. J. Wiskirchen, K. Kraemer, C. König, U. Kramer, J. Trübenbach, A. Wersebe, G. Tepe, K. Dietz, C.D. Claussen, and S.H. Duda. J. Vasc. *Intervent. Radiol*,. 15 (2004) 843.
12. R. Virmani, A. Farb, G. Guagliumi and F.D. Kolodgie. *Coronary Artery Dis*. 15 (2004) 313.
13. E.P. McFadden, E. Stabile, E. Regar, E. Cheneau, A.T.L. Ong, T. Kinnaird, W.O. Suddath, N.J. Weissman, R. Torguson, K.M. Kent, A.D. Pichard, L.F. Satler, R. Waksman, and P.W. Serruys. *Lancet*. 364 (2004) 1519.
14. A.T.L. Ong, E.P. McFadden, E. Regar, P.P.T. de Jaegere, R.T. van Domburg and P.W. Serruys. *J. Am. Coll. Cardiol*. 45 (2005) 2088.
15. J.R. Nebeker, R. Virmani, C.L. Bennett, J.M. Hoffman, M.H. Samore, J. Alvarez, C.J. Davidson, J.M. McKoy, D.W. Raisch, B.K. Whisenant, P.R. Yarnold, S.M. Belknap, D.P. West, J.E. Gage, R.E. Morse, G. Gligoric, L. Davidson, and M.D. Feldman. *J Am Coll Cardiol*. 47 (2006) 175.
16. R. Virmani, G. Guagliumi, A. Farb, G. Musumeci, N. Grieco, T. Motta, L. Mihalcsik, M. Tespili, O. Valsecchi, and F.D. Kolodgie. *Circulation*. 109 (2004) 701.
17. B. O'Brien, J. Stinson and W. Carroll. *Acta Biomater*. 4 (2008) 1553.
18. I.-S. Lee, C.-N. Whang, J.-C. Park, D.-H. Lee and W.-S. Seo. *Biomaterials*. 24 (2003) 2225.
19. K.-W. Kim, E.-H. Lee, J.-S. Kim, K.-H. Shin and B.-I. Jung. *Electrochim. Acta*. 47 (2002) 2525.
20. A. Rossi and J.F.C. Boodts. *J. Appl. Electrochem*. 32 (2002) 735.
21. Y. Murakami, S. Tsuchiya, K. Yahikozawa and Y. Takasu. *Electrochim. Acta*. 39 (1994) 651.
22. Y.E. Roginskaya, O.V. Morozova, E.N. Loubnin, A.V. Popov, Y.I. Ulitina, V.V. Zhurov, S.A. Ivanov, and S. Trasatti. *J. Chem. Soc., Faraday Trans*. 89 (1993) 1707.
23. A. De Battisti, A. Barbieri, A. Giatti, G. Battaglin, S. Daolio and A.B. Boscoletto. *J. Mater. Chem*. 1 (1991) 191.
24. L.A.d. Silva, V.A. Alves, M.A.P.d. Silva, S. Trasatti and J.F.C. Boodts. *Can. J. Chem*. 75 (1997) 1483.
25. ASTM-Standards, *ASTM STANDARDS F640-79 Standard Test Methods for Radiopacity of Plastics for Medical Use*, Annual Book of ASTM Standards, Philadelphia, PA, (2000).
26. S. Habibzadeh, A.A. Khodadadi and Y. Mortazavi. *Sens. Actuators*, B. 144 (2010) 131.
27. S. Habibzadeh, A. Kazemi-Beydokhti, A.A. Khodadadi, Y. Mortazavi, S. Omanovic and M. Shariat-Niassar. *Chem. Eng. J*. 156 (2010) 471.
28. S. Habibzadeh, Y. Mortazavi and A.A. Khodadadi. J. Nanosci. Nanotechnol. 10 (2010) 6003.
29. G.K. Wertheim and H.J. Guggenheim. *Phys. Rev*. B. 22 (1980) 4680.
30. I.D. Belova, T.V. Varlamova, B.S. Galyamov, Y.E. Roginskaya, R.R. Shifrina, S.G. Prutchenko, G.I. Kaplan, and M.A. Sevostyanov. *Mater. Chem. Phys*. 20 (1988) 39.
31. L. Atanasoska, P. Gupta, C. Deng, R. Warner, S. Larson and J. Thompson. *ECS Trans*. 16 (2009) 37.
32. M. Peuckert. *Surf. Sci*. 144 (1984) 451.
33. R.S. Chen, H.M. Chang, Y.S. Huang, D.S. Tsai, S. Chattopadhyay and K.H. Chen. *J. Cryst. Growth*. 271 (2004) 105.
34. L. Atanasoska, R. Atanasoski and S. Trasatti. *Vacuum*. 40 (1990) 91.
35. R. Kotz, H. Neff and S. Stucki. *J. Electrochem. Soc*. 131 (1984) 72.
36. G.G. Kleiman and R. Landers. *J. Electron. Spectrosc. Relat. Phenom*. 76 (1995) 319.
37. J. Friedel. *Adv. Phys*. 3 (1954) 446.
38. J.-C. Dupin, D. Gonbeau, P. Vinatier and A. Levasseur. *Phys. Chem. Chem. Phys*. 2 (2000) 1319.
39. S. Ardizzone, C.L. Bianchi, G. Cappelletti, M. Ionita, A. Minguzzi, S. Rondinini, and A. Vertova. *J. Electroanal. Chem*. 589 (2006) 160.

40. L.A. da Silva, V.A. Alves, S.C. de Castro and J.F.C. Boodts. *Colloids Surf.,* A. 170 (2000) 119.
41. B. Siemensmeyer and J.W. Schultze. *Surf. Interface Anal*. 16 (1990) 309.
42. J. Pouilleau, D. Devilliers, H. Groult and P. Marcus. *J. Mater. Sci*. 32 (1997) 5645.
43. A.A. Marakushev and N.I. Bezmen. *Int. Geol. Rev*. 13 (1971) 1781.
44. C. Angelinetta, S. Trasatti, L.D. Atanososka and R.T. Atanasoski. *J. Electroanal. Chem. Interfacial Electrochem*. 214 (1986) 535.
45. C.-C. Chang, T.-C. Wen, C.-H. Yang and Y.-D. Juang. *Mater. Chem. Phys*. 115 (2009) 93.
46. T. Pauporté and R. Durand. *J. Appl. Electrochem*. 30 (2000) 35.
47. B. Nikolić, V. Panić and A. Dekanski. *Electrocatalysis*. 3 (2012) 360.
48. S. Levine and A.L. Smith. Discuss. *Faraday Soc*. 52 (1971) 290.
49. D. Profeti, T.A.F. Lassali and P. Olivi. *J. Appl. Electrochem*. 36 (2006) 883.
50. S. Trasatti and O.A. Petrii. *J. Electroanal. Chem*. 327 (1992) 353.
51. R. Hang, S. Ma and P.K. Chu. *Diamond Relat. Mater*. 19 (2010) 1230.
52. D. Galizzioli, F. Tantardini and S. Trasatti. *J. Appl. Electrochem*. 4 (1974) 57.
53. S. Ardizzone, G. Fregonara and S. Trasatti. *Electrochim. Acta*. 35 (1990) 263.
54. G.J. Brug, A.L.G. van den Eeden, M. Sluyters-Rehbach and J.H. Sluyters. *J. Electroanal. Chem. Interfacial Electrochem*. 176 (1984) 275.